Aerospace Science and Technology 111 (2021) 106541

Contents lists available at ScienceDirect

Aerospace Science and Technology

www.elsevier.com/locate/aescte

Morphing wingtip structure based on active inflatable honeycomb and shape memory polymer composite skin: A conceptual work

Jian Sun [a,b], Linzhe Du [c], Fabrizio Scarpa [b,*], Yanju Liu [c], Jinsong Leng [a,*]

[a] Center for Composite Materials and Structures, Harbin Institute of Technology, China
[b] Advanced Composites Centre for Innovation and Science (ACCIS), University of Bristol, Bristol, UK
[c] Department of Astronautical Science and Mechanics, Harbin Institute of Technology, China

ARTICLE INFO

Article history:
Received 12 December 2019
Received in revised form 7 November 2020
Accepted 22 January 2021
Available online 26 January 2021
Communicated by Seetha Raghavan

Keywords:
Morphing wingtip
Modeling
Inflatable structure
SMPC skin
Pneumatic muscle

ABSTRACT

Morphing wingtip technology could improve the reduction of the induced drag, fuel consumption, and take-off and landing distances in fixed wing configurations. We describe in this work a morphing winglet concept based on active inflatable honeycombs and Shape Memory Polymer Composite (SMPC) skins. The combination of the two materials and structural subsystems allow the winglet deployment, with a morphing skin able to withstand the aerodynamic loading, also through the use of distributed pneumatic muscle fibers. An actuation geometric and mechanical model that represents the morphing wingtip concept is developed and analyzed. A morphing wingtip prototype is also fabricated to demonstrate the kinematics and actuation of the concept. Experiments and simulations show agreement about the output angle/input pressure relationship necessary for the wingtip deployment.

1. Introduction

Morphing wing technologies for aircraft designs are receiving significant attention within the aerospace R&D community due to their potential benefits to extend the flight envelope of classical fixed-wing aircraft [1,2]. Biomimetic structures [3–8] are put forward and optimized to get better performance in morphing area. A morphing wingtip technology could bring several improvements on the overall performance of an airplane [9,10]. The lift to drag ratio during climb could be improved by the change of the wing span length, and vertex-induced drag during high-speed flight could be reduced by the folding of the wingtip. Studies show the morphing wingtip structure could improve 25.32% of lift coefficient (C_l) [11] and save 5% fuel [12]. In fact, besides fuel reduction, the improvement of lift coefficient will benefit more. The higher lift coefficient means more lead ability, which means more sensors or weapons. The maneuverability could also be improved by assisting the control of ailerons, elevators and rudders, much like birds' wings, and fuel consumption may be adaptively reduced in High Altitude Long Endurance flights [13]. Moreover, a morphing wingtip could be used to extend the range of airports available for operations for a given aircraft, much like Boeing 777X design. However, the joint on 777X's wingtip is bare without skin. And the juts outside would increase drag and cause aerodynamic damage. Current morphing wingtip designs are based on motor actuation [14,15], inflatable systems [16] and use of new smart materials and structures, including inflatable honeycombs [17], multistable structures [18,19] and Shape Memory Alloys (SMA) [20].

Honeycombs have been extensively used in wingbox and skin design [21–24] because of high bending stiffness per unit weight and specific transverse shear stiffness. Cellular structures such as zero Poisson's Ratio honeycomb [25] can also provide large in-plane morphing configurations when applied to wind turbine blades [26], span-wise [27–29] and chord-wise morphing [30,31], as well as variable camber wing configurations [32]. Active actuation is a relatively novel new feature in cellular structures. One way to obtain an active honeycomb configuration is to fabricate the cellular structure itself with active materials such as Shape Memory Alloy (SMA) [33,34] or Shape Memory Polymers (SMP) [35]. Attempts in the past have also been made to insert in the cell ribs distributed actuators, both for dynamic shape morphing and sensing/structural health monitoring applications [36,37]. Another actuation strategy adopted in morphing honeycombs consists in using a pressurized fluid within the honeycomb cells. The shape of the honeycomb can be therefore controlled by applying either uniform [38] or differential pressures at different cells [39,40]. Hy-

* Corresponding authors.
E-mail addresses: f.scarpa@bristol.ac.uk (F. Scarpa), lengjs@hit.edu.cn (J. Leng).

https://doi.org/10.1016/j.ast.2021.106541

Nomenclature

R_0	Initial outside radius of a tube
θ	Angle between two straight walls of one honeycomb
a_1	Length of the lower oblique wall of a honeycomb unit cell
a_2	Length of the upper oblique wall of a honeycomb unit cell
b	Length of straight wall of the honeycomb unit cell
h	Distance between the center of tube and intersection of the lines related to straight honeycomb cell walls
θ_{max}	Maximum angle between two straight walls of one honeycomb
α	Lower angle between oblique and straight honeycomb walls
β	Top angle between oblique and straight honeycomb walls
c	Length of the contact surface between straight honeycomb cell walls and tube
r_1	Outside radius of lower circular arc
r_2	Outside radius of upper circular arc
ρ_1	Central radius of the lower arc unit
M_1	Moment on the two sides of lower arc unit
F_{t1}	Shearing force on the two sides of lower arc unit
t	Thickness of the tube
E	Young's modulus of the tube material
I	Rotary inertia of the arc unit about normal direction of the section
w	Width of the honeycomb and tubes
F_{t0}	Shearing force on the two sides of lower arc unit while the tube is a circle
F_1	Recovery force of lower arc
F_2	Recovery force of upper arc
K	Stiffness of the honeycomb structure
P_{top}	Uniform pressure applied on the top of the honeycomb structure
A_{top}	Area of the top surface of the honeycomb structure
d	Vertical displacement of the middle beam of the honeycomb structure
Φ	Wingtip angle
P	Input pressure to the internal surface of the tubes
G	Extra loading applied on the end of the wingtip
G^*	Equivalent loading of self-weight of the wingtip
L	Length of the wingtip

draulic tubes can also be sandwiched within the honeycomb lattice or inserted in segmented structures, such as in biomimetic beam-steering antenna concepts [41,42], robotic platforms [43,44] and prosthetic hands [45].

For a morphing structure, a compliant and adaptive skin is an important component [46]. A morphing skin should not only supply a deformable aerodynamic surface, but also be able to withstand the load on a wing. Elastomer [47–49] and inflatable skins [50,51] can supply large deformations for morphing, but low stiffness for loading-bearing capability. Segmented [52,53] and corrugated structures [54,55] are adaptive and provide both out-of-plane stiffness and tailorable in-plane compliance, but do not provide a smooth external surface. Therefore, novel variable stiffness materials are needed to meet the conflicting requirements of a morphing skin [56]. Shape Memory Polymers (SMP) are considered a variable stiffness material controlled by temperature [57]. The SMP skins alter shape, with their microstructure in rubbery state at low stiffness, and can withstand aerodynamic loads in the glassy state with high stiffness. SMP skins have been already evaluated for morphing chord wings [58], folding [59], deployable [60], and variable camber wings [61,62].

This paper describes a morphing wingtip structure based on an active honeycomb configuration and a SMPC skin. The honeycomb configuration is actuated by inflating tubes with a volumetric expansion [63–65]. The type of honeycomb considered in this work has the re-entrant (butterfly) configuration that provides an in-plane negative Poisson's ratio behavior [66]. An approximate analytical model is developed to describe the geometry parameters and the mechanical properties of the active inflatable-SPMC system. Pneumatic muscle fibers have been also recently evaluated as lightweight, low-cost and efficient actuators to provide axial thrust, and they also have been found to resist bending moment [65,66]. Pneumatics tube and actuators may be therefore considered to offer a stiffening effect to the SMPC skin. A reduced-scale demonstrator of the active honeycomb concept has also been produced, showing a general satisfactory agreement with the predictions provided by the model. The SMPC skin used has the same microstructure configuration shown in [62], with 20% volume of polyurethane fiber enhanced styrene-based shape memory polymer composites. The 2 mm-thickness SMPC skin covers the whole morphing wingtip structure, and shows promise for further potential applications, especially for UAVs designs.

2. Morphing wingtip concept

Fig. 1(a) shows the baseline morphing wingtip structure design that includes a fixed wingbox, fixed wingtip, hinge, the re-entrant (butterfly) honeycomb, the inflatable tubes and the Shape Memory Polymer Composite (SMPC) skin. The honeycomb shape could change with the inflation of the structure, and at the same time maintain the aerodynamic load transfer from the skin to the rest of the wingtip configuration. The SMPC skin provides an external smooth wing surface that becomes compliant in its rubbery state, and car resist the aerodynamic loading in its glassy state. The operational behavior of the morphing wingtip is described as follows:

(1) The wingtip rests in a deployed state with a larger physical aspect ratio wing (shown as Fig. 1(a)) during take-off and climb phases. The lift/drag ratio can be improved for shorter takeoff distances.
(2) When the configuration of the wingtip needs to be changed (i.e., flap-up to reduce the induced drag or modify the roll rate) the SMPC skin should be heated to decrease its stiffness. No input pressure to the tubes is applied, but the wingtip flaps up under the pressure differential between the upper and lower surface of the wing. After reaching the designed final position, the SMPC skin is cooled down to become stiff to form a stable winglet configuration, (Fig. 1(b)).
(3) The wingtip can again deploy based on the operational flight requirements, and in that case the tubes are inflated after the SMPC skin has been heated up. With a subsequent cooling of the skin temperature, the deploy wingtip configuration is fixed.

3. Modeling

3.1. Geometric model

The configuration proposed in this work is based on the use of two butterfly-shaped (auxetic) cellular units in mutual constant

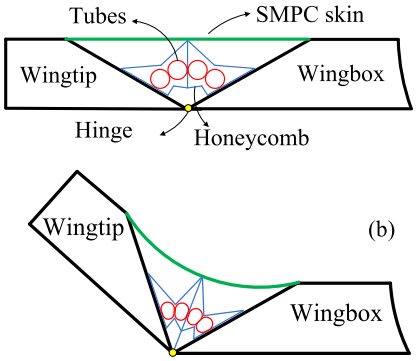

Fig. 1. Morphing wingtip concept. (a) Structural layout of the morphing wingtip; (b) Flap- up state.

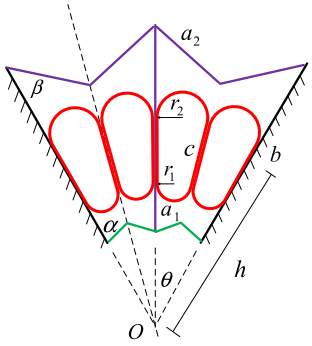

Fig. 2. Geometric model of the active honeycomb.

contact with the left and right sides fixed [17]. The configuration is shown in Fig. 2. Two compressed tubes are installed inside each honeycomb cell. The center of the contact surface between the straight cell walls of the honeycombs and the tube coincides with the center of the honeycombs straight wall. There are some assumptions in the design proposed:

1. The two butterfly cellular structures and the internal tubes are equal and symmetric with respect to interface line between the two tubes.

2. The line connecting the centers of the two arcs intersects the two straight cell walls at point O. The section of a tube is symmetric with respect to this line.

3. There is no sliding between the tubes and the honeycomb walls, i.e. the parameter 'h' in Fig. 2 is a constant.

For given values of R_0 and θ_{max}, the allowable intervals of h, a_1, a_2, and b can be obtained from the following relationships:

$$h \le R_0 / \tan(\theta_{\max}/4) \tag{1}$$

$$a_1 \ge (h - b/2)\sin(\theta_{\max}/2) \tag{2}$$

$$a_2 \ge (h + b/2)\sin(\theta_{\max}/2) \tag{3}$$

$$2h \ge b \ge a_1 + a_2 \ge 2h\sin(\theta_{\max}/2) \tag{4}$$

By assuming $R_0 = 2.75$ mm and $\theta_{max} = 60$ degree, the inequality $h \le 10.26$ mm is obtained from equation (1) and 20 mm $\ge b \ge$ 10 mm from equation (4). Fig. 3 shows the acceptable a_1 and a_2 intervals versus the parameter b for $h = 10$ mm. The geometric parameters can be selected from the shaded area, i.e. $b = 16$ mm, $a_1 = 3$ mm, $a_2 = 11$ mm, these parameters are used in the following analysis and design.

The angles of the honeycomb cells can be described by the angle θ (Fig. 4):

$$a_1 \sin\alpha = \tan(\theta/2)(h - b/2 + a_1\cos\alpha) \tag{5}$$

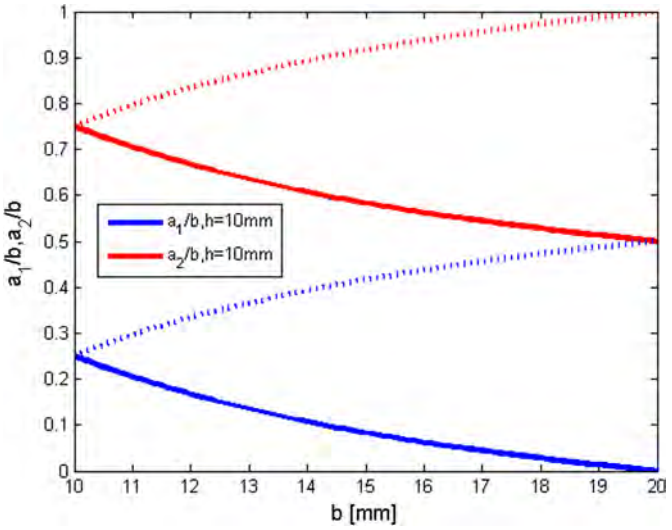

Fig. 3. Allowable design envelopes for a_1 and a_2.

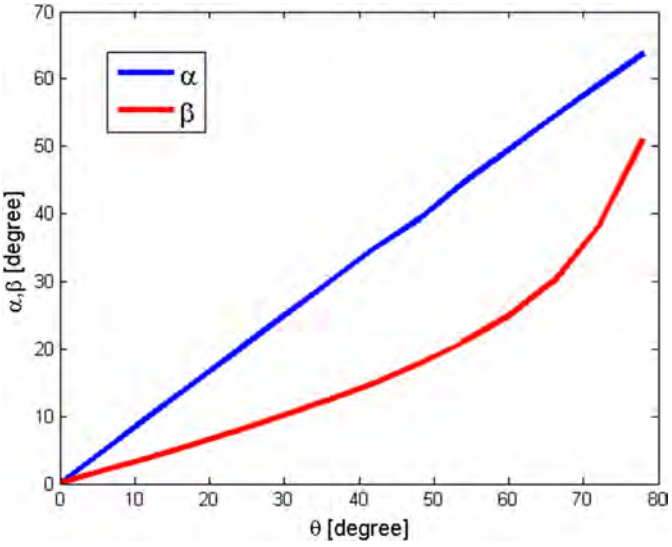

Fig. 4. Curves of α and β versus θ.

$$a_2 \sin\beta = \tan(\theta/2)(h + b/2 - a_2\cos\beta) \tag{6}$$

The required geometric dimensions of the tubes are discussed in detail in reference [17]:

$$c = \frac{\pi R_0 - \pi h \tan\left(\frac{\theta}{4}\right)}{1 + \frac{\theta}{4}\tan\left(\frac{\theta}{4}\right)} \tag{7}$$

$$r_1 = \frac{h - c/2}{h + c/2} r_2 \tag{8}$$

$$r_2 = \left(h + \frac{c}{2}\right)\tan\left(\frac{\theta}{4}\right) \tag{9}$$

3.2. Mechanical model of the tube

The model of the actuating tube is based on the one reported in former study [68]. Fig. 5 shows the cross-section of a single tube. The recovery force is referred to the compressed tube. It is also assumed that the tube has a flat configuration in the original state, and then becomes a doubled curved arc profile with a pair of shearing forces (F_{t1}).

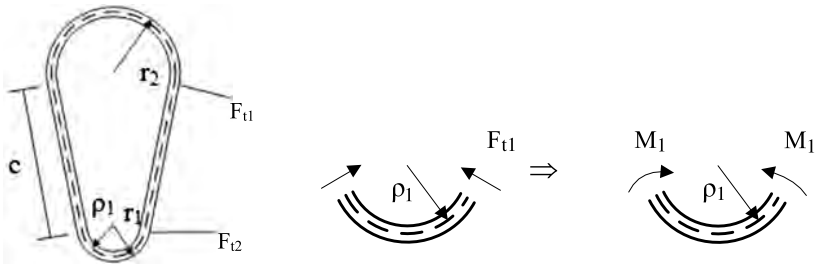

Fig. 5. Mechanical model of one tube.

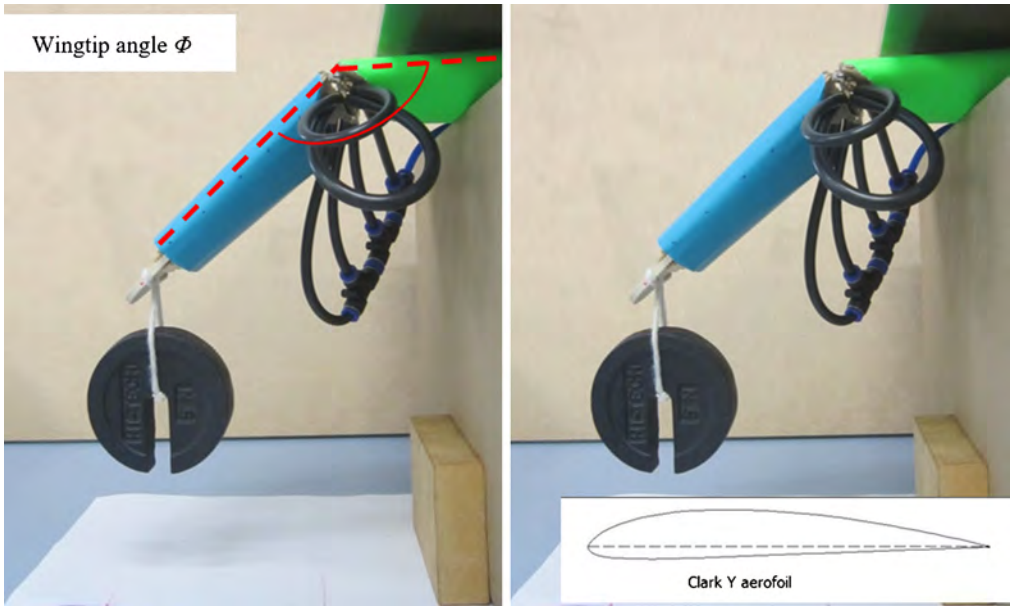

Fig. 6. Experimental setup of the morphing wingtip structure demonstrator. (For interpretation of the colors in the figure(s), the reader is referred to the web version of this article.)

According to Saint-Venant's principle [66], the shearing force on the two sides of the lower arc creates a moment about the normal direction of the section (Fig. 5):

$$M_1 = F_{t1}\rho_1 \cos\left(\frac{\theta}{4}\right) \tag{10}$$

where $\rho_1 = r_1 - \frac{t}{2}$. If pure bending occurs within the walls of the tube, the moment can be represented as:

$$\frac{1}{\rho_1} = \frac{M_1}{EI} \tag{11}$$

where the moment of inertia about the normal direction of the section is $I = \frac{wt^3}{12}$. From equations (10) and (11), the shearing force F_{t1} can be obtained as:

$$F_{t1} = \frac{EI}{\left(r_1 - \frac{t}{2}\right)^2 \cos\left(\frac{\theta}{4}\right)} \tag{12}$$

The original shape of the tube is circular, which implies the presence of an internal pre-stress. Therefore, the recovery force of the lower arc of the tube is composed by the shearing force obtained when inflating the tube, minus the original shearing force present in the original configuration:

$$F_1 = (F_{t1} - F_{t0}) = \frac{EI}{\cos\left(\frac{\theta}{4}\right)}\left(\frac{1}{\left(r_1 - \frac{t}{2}\right)^2} - \frac{1}{\left(R_0 - \frac{t}{2}\right)^2}\right) \tag{13}$$

Using a similar approach, the recovery force on the upper arc of the inflated tube can be obtained as:

$$F_2 = \frac{EI}{\cos\left(\frac{\theta}{4}\right)}\left(\frac{1}{\left(r_2 - \frac{t}{2}\right)^2} - \frac{1}{\left(R_0 - \frac{t}{2}\right)^2}\right) \tag{14}$$

3.3. Experiments and discussions

A reduced scale demonstrator of the morphing wingtip concept has been produced following a baseline Clark YM-18 as airfoil (Fig. 6). The wingtip and wingbox structures are made from an airfoil-shaped 4 mm-thickness wooden plate, with the ends combined with 2 mm-thickness wooden skin. Foam (Cam-Spares Bryan McCansh 19, West Drive, Ferring Worthing West Sussex BN12 5QZ United Kingdom) is filled inside the wing cavity. The wingbox and the wingtip are connected through a hinge that fixed the equilibrium position of the wingtip and fixed wing structure at an angle of 120°. A butterfly (re-entrant) honeycomb structure made of PEEK film (0.2 mm thickness, Aptiv 1000 film, Victrex, UK) following a Kirigami manufacturing process is bonded by adhesive (Epoxy 330 Water Clear Adhesive Lapidary Rock Gem Glue Cement Jewelers) between the fixed wingbox and the wingtip. Two tubes are installed inside each honeycomb. The tubes are made of polyvinyl chloride (PVC, Shenzhen Longxiang Electronic co., LTD, China, thickness: 0.84 mm, outside diameter: 5.5 mm). The weight of the demonstrator is about 450 g and the envelope size is about 150 cm $*$ 300 cm.

In Fig. 6, the simulacre of the wingbox (green) is fixed, and the one of the wingtip (blue) is hinged at an equilibrium position. The wingtip has its own weight G^*. To simulate an equivalent concentrated load G provided by an external pressure an extra loading

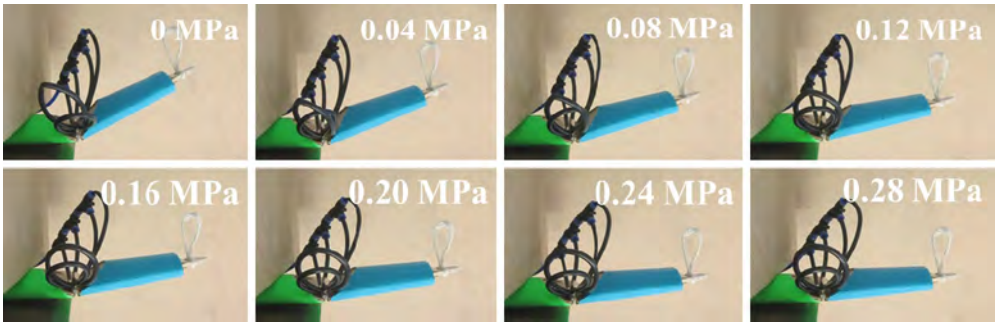

Fig. 7. Simulacra of the morphing of the wingtip configuration without shape memory polymer skin and with black inflatable tubes at different input pressures.

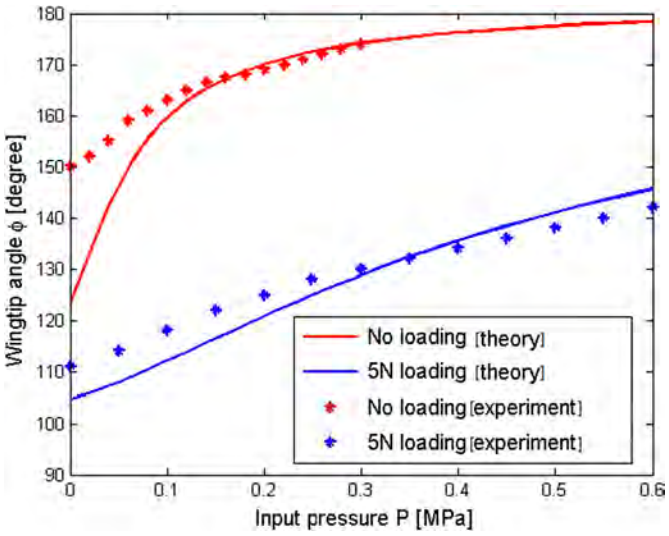

Fig. 8. Wingtip angle versus input pressure from experiments and model results.

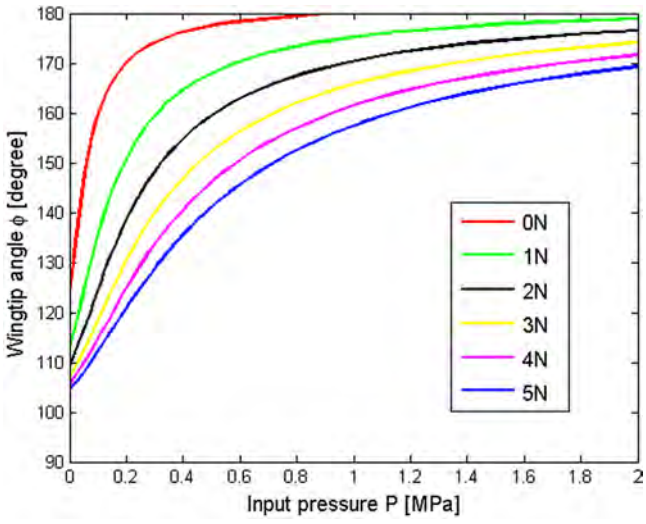

Fig. 9. Theoretical wingtip angle versus the input pressure for different external loading values.

(5N) is appended at the end of the wingtip. The deployment of the morphing wingtip without the appended load is shown in Fig. 7. No shape memory polymer skin is applied in this case. The wingtip angle Φ is measured by Adobe Photoshop using the images record by a camera (Canon EOS Rebel SL1). It is evident that the wingtip angle Φ increases (i.e. the wingtip tends to assume a horizontal configuration) with higher input pressure inside the tubes.

From the balance of the external moments on the whole structure one obtains:

$$F_2\left(h+\frac{c}{2}\right)+F_1\left(h-\frac{c}{2}\right)+Pcwh=\left(G+G^*\right)L\cos\left(\pi-\Phi\right) \quad (15)$$

where $\Phi=\frac{\pi}{3}+\theta$, $G^*=0.6$ N, $L=140$ mm, $w=40$ mm, $h=10$ mm.

Combining equations (13) and (14) with the relation in (15), it is possible to obtain the value of the wingtip angle Φ versus the input pressure P and compare it against the experimental results (Fig. 8). In general, the model tends to overestimate the angle at very low input pressures, in particular when no external load is present. It is apparent that the initial static deformation of the experimental winglet model when no weight is appended cannot be adequately adjusted by low pressure inputs below 0.2 MPa, also due to contact friction effects existing between the tubes and the cellular configurations that are difficult to overcome at low inflation pressures. At higher pressure levels, these effects are less strong, and the model gives a more satisfactory agreement. When an external loading is applied the effects of the initial static deformation and internal hysteresis in the wingbox-winglet system is less pronounced, and in general the model shows maximum discrepancies with the experiments close to 4.5%. Fig. 9 shows the behavior of the wingtip angle and the input pressure at different external loadings using the benchmarked model. It is intuitive to ascertain that larger input pressures with high wing loading are needed to deploy the winglet for a specific angle.

A second demonstrator is produced covering the pneumatic-actuated morphing wingtip structure with a 20 vol% elastic fiber enhanced SMPC skin [67]. The Young's modulus of the skin is close to 650 MPa in glassy state, and less than 3.3 MPa in the rubbery phase. Fig. 10 provides a view of the deployment of the prototype. A hot blower gun is used to heat the skin. The output temperature is about 300 °C. When the skin is heated the SMPC transforms into a rubbery state from the initial stiff configuration. The skin will then deform following its shape memory characteristics to reach the required shape change. The skin maintains a smooth external surface for the wing, with no final gaps or evident wrinkling/corrugations at the end of the whole morphing process.

We can find that in Fig. 10, there is a wrinkle between wing and wingtip. The influence of the wrinkle must be figured out. Fluent (ANSYS) is used to simulate the aerodynamic of the wrinkle. The model is made by SolidWorks as shown in Fig. 11. The NASA0012 airfoil profile is adapt. The length of wing is set as 7 m and the wingtip takes 1 m of the total wing length. The angle of wingtip is 60 degree. A 'V' shape wrinkle is made between them. The angle of V-wrinkle is 58.15 degree and the position is symmetry. The air filed is made by 20 m ∗ 20 m ∗ 20 m. the whole mesh size is 0.5 m and the boundary layer size is 0.05 m. 5 boundary layers is set.

Using a total speed of 100 m/s and 6 attack angle, we get the drag coefficient (C_d), lift coefficient (C_l), lift-drag ratio as Table 1. And the speed field in the middle of wing also shows in Fig. 12.

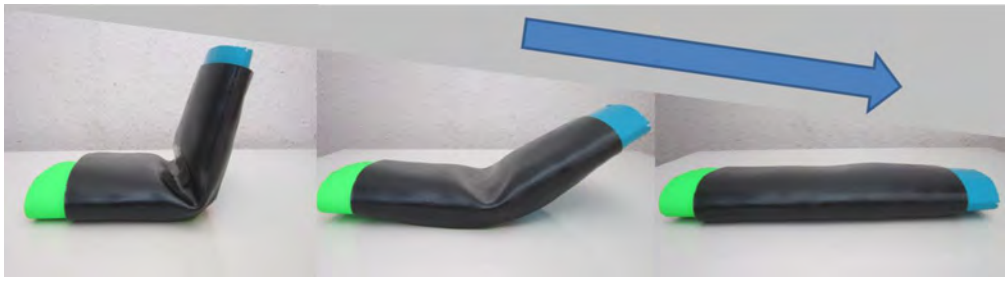

Fig. 10. Deployment of the wingtip demonstrator with the SMPC skin.

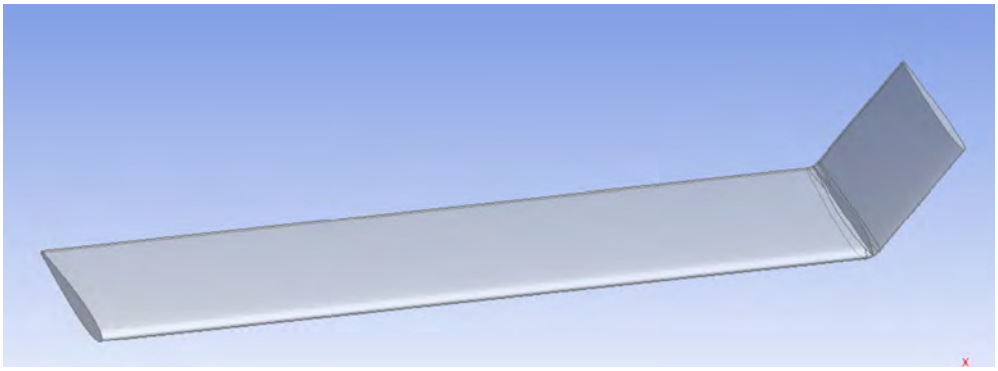

Fig. 11. The wingtip model with a V-wrinkle.

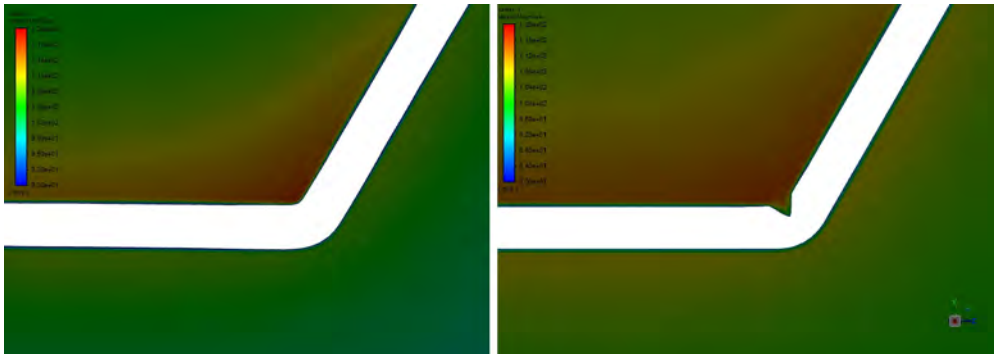

Fig. 12. The wingtip model with a V-wrinkle.

Table 1
The aerodynamic comparison of wrinkle wingtip and non-wrinkle wingtip.

	Folding Wingtip with wrinkle	Folding Wingtip without wrinkle	Difference
C_l	0.062405	0.063198	−1.25%
C_d	0.005439	0.005705	−4.66%
C_l/C_d	11.47268	11.07745	+3.57%

It can be found that compared with unwrinkled wing section, the wrinkle wing's C_l has declined by 1.25%, but the C_d is also reduced by 4.25%, which together leads to 3.57% increased lift-drag ratio. The simulation shows that the wing with wrinkle has little difference to the unwrinkled one and even a little better in some cases.

4. Morphing skin stiffening using pneumatic muscle fibers (PMFs)

The use of SMPC only as external skin is problematic because the stiffness of the skin in rubbery is too low to bear external pressures. A possible way to increase the stiffness while maintaining morphing capabilities is the use of pneumatic muscle fibers (PMF) connected to the SMPC via direct bonding [69]. When the SMPC skin is heated, the muscle fibers are inflated and provide the additional support. The pneumatic muscle fibers (Mckibben type [70]) have been produced by using medical rubber hose (inner diameter 1.5 mm, outer diameter 2.5 mm, latex) and woven nets (nylon). The length of the PMF is variable, but no less than 3 cm.

Finite Element (FE) simulations have been performed to verify the design solution prospected for the support of the SMPC skin. Data from anti-bending tests are used to define equivalent displacement-forces curves for the material constituting the PMF in the FE models. Fig. 13 shows the experimental facility used for the anti-bending tests; the fixing and connecting devices are not shown in the figure. A laser displacement sensor (LVD) is used to measure the displacement. The PMFs tested had a length of 21 cm and external radiuses of 3 mm. Fig. 14 shows the results from the tests. It is evident the presence of a substantial linear response between external load and output displacement for the highest inflatable pressure used here (0.35 MPa). For lower pressure values the displacements are higher, and follow a softening curve with the increase of the concentrated load.

The pneumatic muscle fibers are modeled as elastic tangible beams within the FE model. This simplification leads however

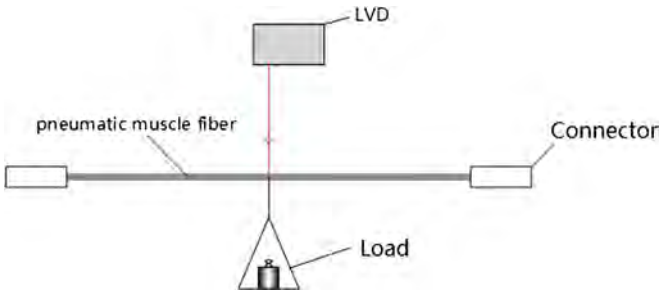

Fig. 13. Anti-bending experiential facility.

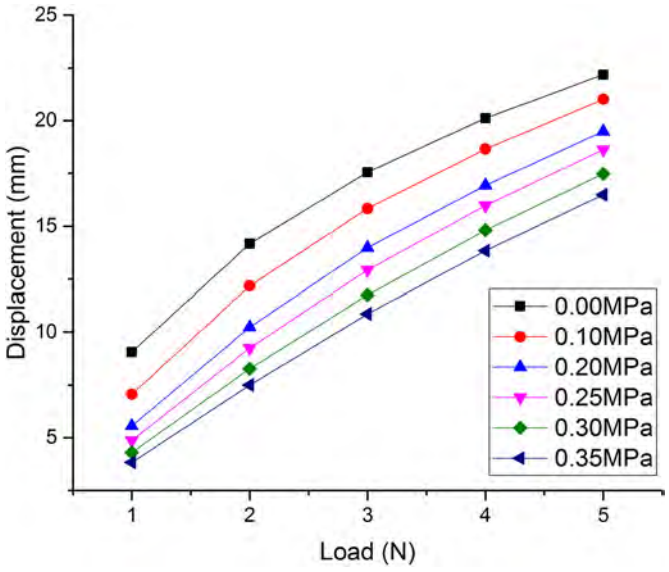

Fig. 14. Anti-bending experimental results.

Table 2
Material constants for the pneumatic muscles and SMP [62].

Material	Young modulus [MPa]	Poisson's ratio
Pneumatic muscle fibers	Using test data	0.3
SMP in glass state	*651.99*	*0.35*
SMP in rubber state	*3.26*	*0.35*

lower final deformations during the shape changing process. To enhance the contact between the SMPC and the pneumatic muscles, the cross-section of the latter is tapered, so the face-to-line contact turns into face-to-face contact (Fig. 15a). The engineering material constants used in the models are listed in Table 2. The size of the skin considered here is 134 mm $*$ 134 mm $*$ 2 mm. Because the skin cannot keep in contact with the PMFs at the beginning in the actual operation, the gap between SMP skin and PMFs is set as 2.92 mm (as measured experimentally in the rig described later).

For the meshing of the model, different strategies have been adopted to discretize the SMPC and the PFM parts (Fig. 15). A C3D8RH element class is used for the SMPC skin. The PFM parts are solid modeled with a sweep technique resulting into 4-mm size C3D8RH elements. The whole model (skin plus PMF stringers) consisted in 640 elements. Clamping boundary conditions are applied and an external pressure of 1.3 kPa is applied to the SMPC skin to simulate the wing at a speed of 46.5 m/s on the ground according to Bernoulli equation. The Abaqus/Standard solver is used to perform the simulations. The Nonlinear Geometric (Nlgeom) is actived in simulation. And the plantform is I5-2430, 8G RAM, Windows 10.

Table 3
Maximum displacements of the SMPC system in different states.

State	Maximum displacement [mm]
Glass state without PMF	1.827
Glass state with PMF	1.827
Rubber state without PMF	11.52
Rubber state with PMF	5.626

The results of the FE simulations are shown in Fig. 16. It is possible to observe that the deformation patterns differ significantly between the glass and rubber states. The skin essentially behaves as a single rigid plate in the glass phase, and when heated the rigidity decreases and assumes therefore a more membranal behavior, with both bending and shear stiffness reduced. The resulting maximum displacement of the plate is increased by a factor of 5.3 when passing from glassy to rubbery state (Table 3). The pneumatic muscle fibers act as stiffeners for the SMPC plate, and this is particularly noticeable when the SMPC is in rubber state; the displacement of the skin with the PMF stringers is in this case two orders of magnitude lower compared to the configuration without the pneumatic fiber muscles.

To verify the simulations performed, a specific test protocol has been put in place (Fig. 17). A lidless box made of four pieces of Acrylic and SMPC plate is fixed and filled with water. Under the SMPC plate three pneumatic muscle fibers are fixed to barriers. Hot water (70 °C) is poured into the box to give an hydrostatic pressure to the SMPC and turn the SMPC bottom from the glassy state to the rubber state at the same time. A thermometer is put into the water to track the temperature and ascertain whether it is always above 65 °C, so that the SMPC is in rubber phase. A laser displacement sensor (LVD) is fixed below the box to measure the displacement of the SMPC plate.

During the test the pneumatic muscle fibers are inflated with an atmospheric pressure of 0.3 MPa. The hydrostatic depth of the water varied from 0.5 kPa to 1.3 kPa and the displacement of the SMPC plate was recorded. The measure points on SMPC plate are set where the maximum displacement take place according to the previous FE simulations. The results of the experimental tests are shown in Fig. 18. It is worth noticing here that the presence of the PMFs changes the magnitude of the output displacements, but not the overall trend that defines increasing displacements for higher input pressures. The PMFs provide a 63% reduction of the deformation of the SMPC skin across the pressure ranges exerted here. A comparison between the experimental and numerical results is shown Fig. 19. One can notice a general agreement in terms of dependency of the maximum displacement versus input pressure. The FE model provides a linear response, with maximum errors up to 14%. The discrepancies are more significant at low and high input pressures. Possible reasons behind the incongruities are the exact determination of the gap between the skin and the fibers, and manufacturing uncertainties associated to the production of the PMFs used in the development of the stiffened SMPC plates. The results however show the model could be used to estimate general design trends and provide a conservative response for the structural morphing system.

Above experiments shows the validity of the simulation. But the deformation is still too large for engineering applications. In fact, instead of pure SMP, reinforced SMP composite is the common role in practical use. If we use carbon fiber (TORAYCA's T300 product, Tensile modulus is 230 GPa) as 10% reinforcement into SMP, and reduce the distance of pneumatic fiber muscles from 33.5 mm to 16.75 mm, using the same model, the max displacement could reduce to 2.463 mm and 2.507 mm in glass state and rubber state. If we accept Jacob's result [71] that the deformation

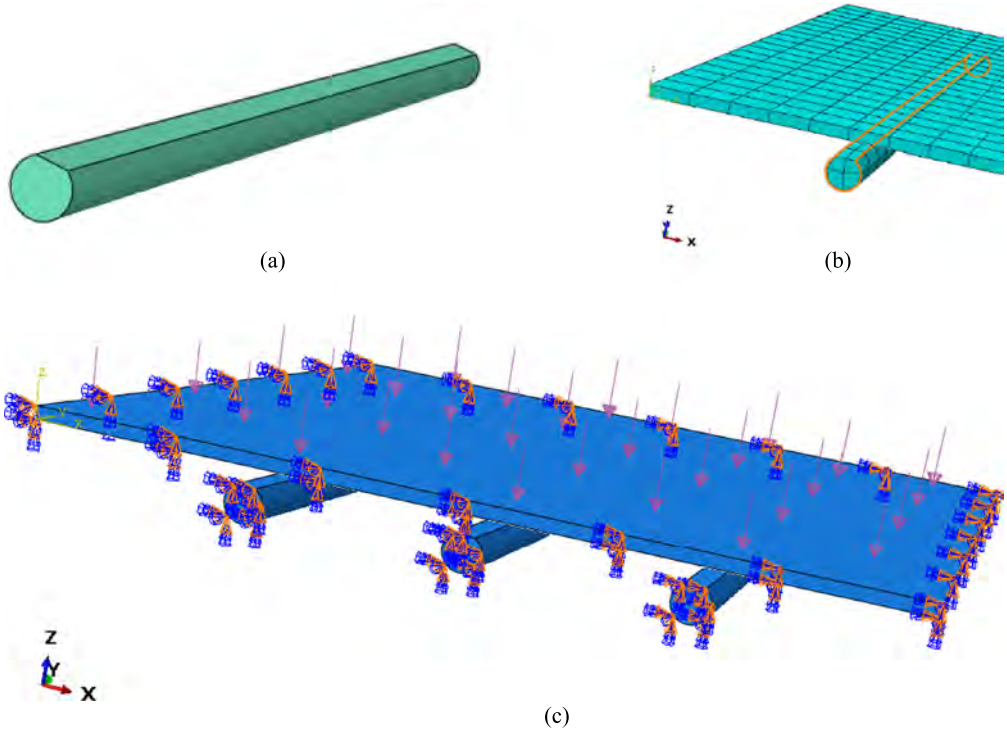

Fig. 15. (a) Solid model representing the PMF part, (b) its FE mesh and (c) boundary conditions and loads applied.

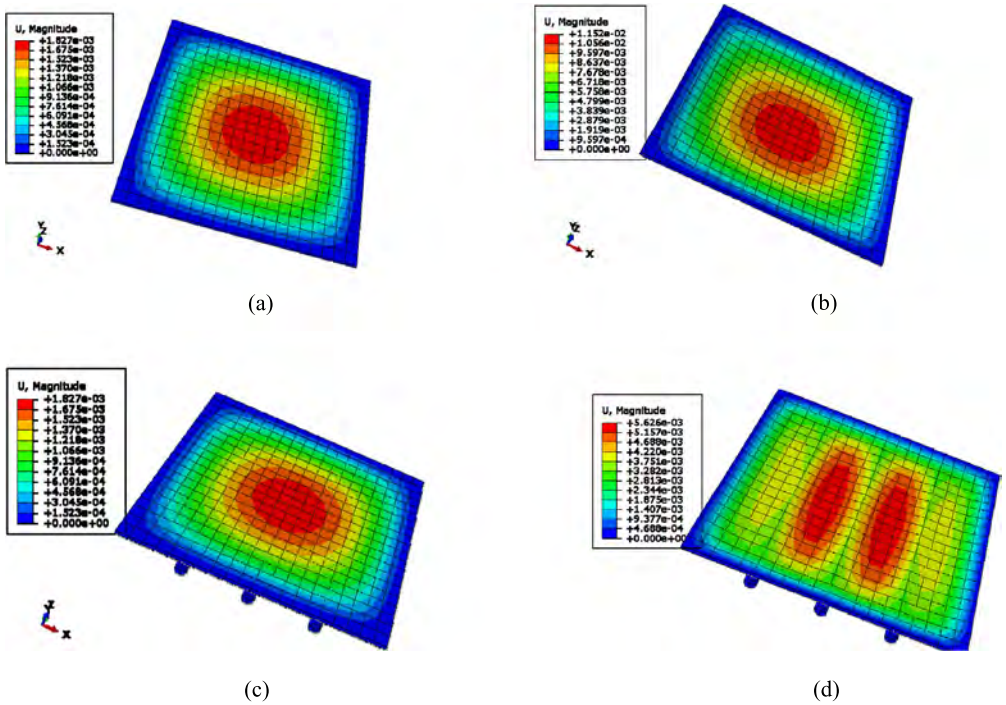

Fig. 16. Contour deformations plots for the SMPC skin in (a) glass state without PMFs; (b) rubber state without PMFs; (c) glass state with the PMFs and (d) rubber state with the PMFs.

can be ignored in aeroelastic analysis if the max displacement is less than 0.1% chord, our demo is suit with UAVs with wing chord bigger than 30 cm. Besides, there are many other methods to enhance the structure, for example, increase the size of pneumatic fiber muscles, increase the pressure of pneumatic fiber muscles, increase thickness of SMP skin and so on. Engineers can choose either those methods to enhance their structures as their own needs.

5. Conclusions

This paper has described the concept of a morphing wingtip based on the use of an active deployable honeycomb based on pneumatics actuation and a shape memory polymer/carbon skin. The geometrical configuration and the mechanical performance of the active honeycomb under compression was modeled. The input pressure/wingtip angle relationship for the morphing wingtip sys-

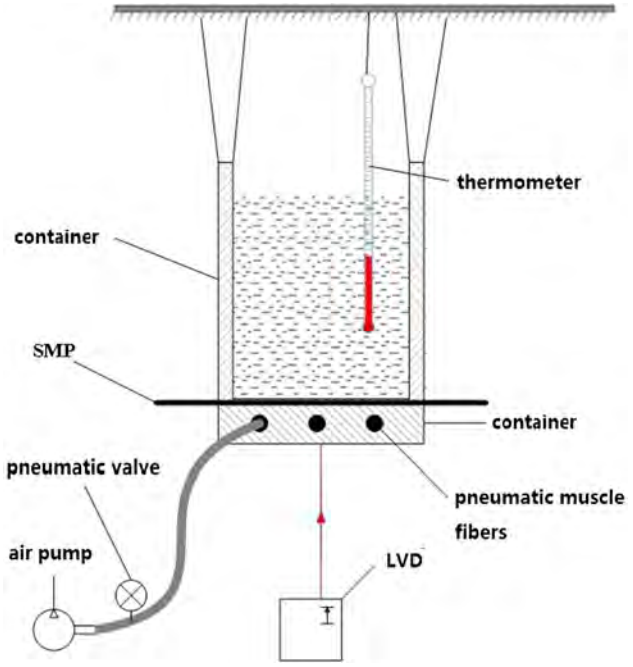

Fig. 17. Testing apparatus to verify the load bearing capacity of the SMPCs with and without pneumatic muscle fibers.

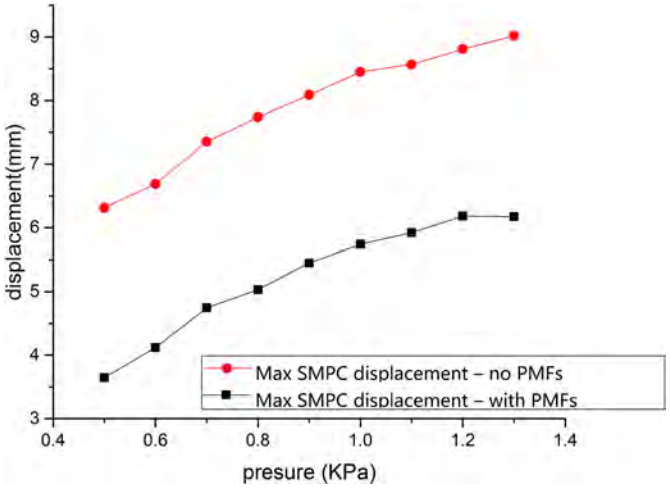

Fig. 18. SMPC maximum displacements with and without PMF stringers at different input pressures.

tem was also obtained, and verified in a specific test sample. A simulacre of morphing wingtip was fabricated and its performance showed a good agreement with the theoretical framework developed. The demonstrator has shown the feasibility of this concept for possible morphing wingtip configurations for further application. Pneumatic fiber muscles have been developed as adaptive stiffeners to adjust the bending and membrane stiffness of the shape memory polymer skin during deployment. The operational effectiveness of the stiffened SMPC plate was verified by experimental tests produced in an ad-hoc rig, and Finite Element models that provided a good agreement with the experimental trends measured. The concept described in this paper may be further evaluated for the use of small UAVs, or for other adaptive structures designs in which shape memory polymers could find their use, e.g. [72].

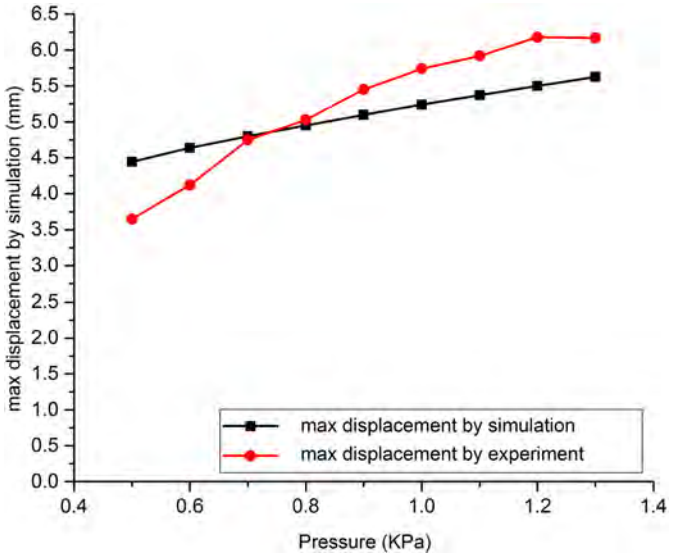

Fig. 19. Maximum displacement comparison between simulations and experiment for the shape memory polymer/carbon skin with the pneumatic fiber muscles.

Declaration of competing interest

The authors declare that they have no known competing financial interests or personal relationships that could have appeared to influence the work reported in this paper.

Acknowledgements

This work was supported by the National Natural Science Foundation of China (Grant No. 11802076, No. 11632005), and "the Fundamental Research Funds for the Central Universities" (Grant No. HIT. NSRIF. 201822). J. Sun would also like to thank CSC (Chinese Scholarship Council) for funding his research work at the University of Bristol. FS is also grateful to the European Commission for the FP7-AAT-2012-RTD-L0-341509 MorpheElle project that provided the infrastructure logistics of the activities described in this paper.

References

[1] S. Barbarino, O. Bilgen, R.M. Ajaj, M.I. Friswell, D.J. Inman, A review of morphing aircraft, J. Intell. Mater. Syst. Struct. 22 (2011) 823–877.
[2] J.C. Gomez, E. Garcia, Morphing unmanned aerial vehicles, Smart Mater. Struct. 20 (2011) 103001.
[3] D.A. Burdette, J.R.R.A. Martins, Design of a transonic wing with an adaptive morphing trailing edge via aerostructural optimization, Aerosp. Sci. Technol. 81 (2018) 192–203.
[4] Z. Hui, Y. Zhang, G. Chen, Aerodynamic performance investigation on a morphing unmanned aerial vehicle with bio-inspired discrete wing structures, Aerosp. Sci. Technol. 95 (2019) 105419.
[5] I. Mir, A. Maqsood, S.A. Eisa, H. Taha, S. Akhtar, Optimal morphing – augmented dynamic soaring maneuvers for unmanned air vehicle capable of span and sweep morphologies, Aerosp. Sci. Technol. 79 (2018) 17–36.
[6] D. Xu, Z. Hui, Y. Liu, G. Chen, Morphing control of a new bionic morphing UAV with deep reinforcement learning, Aerosp. Sci. Technol. 92 (2019) 232–243.
[7] B. Yan, P. Dai, R. Liu, M. Xing, S. Liu, Adaptive super-twisting sliding mode control of variable sweep morphing aircraft, Aerosp. Sci. Technol. 92 (2019) 198–210.
[8] Y. Zhang, J. Zhao, W. Chen, X. Guo, S. Yan, G. Hu, Y. Yuan, P. Guo, Q. Cai, Biomimetic skeleton structure of morphing nose cone for aerospace vehicle inspired by variable geometry mechanism of honeybee abdomen, Aerosp. Sci. Technol. 92 (2019) 405–416.
[9] D.D. Smith, R.M. Ajaj, A.T. Isikveren, M.I. Friswell, Multi-objective optimization for the multiphase design of active polymorphing wings, J. Aircr. 49 (4) (2012) 1153–1160.
[10] P. Bourdin, A. Gatto, M.I. Friswell, Aircraft control via variable cant-angle winglets, J. Aircr. 45 (2) (2008) 414–423.

[11] L. Falcão, A.A. Gomes, A. Suleman, Aero-structural design optimization of a morphing wingtip, J. Intell. Mater. Syst. Struct. 22 (10) (2011) 1113–1124, https://doi.org/10.1177/1045389X11417652.
[12] P. Marks, "Morphing" winglets to boost aircraft efficiency, New Sci. 201 (2692) (2009) 22–23, https://doi.org/10.1016/S0262-4079(09)60208-6.
[13] Mayuresh J. Patil, Dewey H. Hodges, Carlos E.S. Cesnik, Nonlinear aeroelasticity and flight dynamics of high-altitude long-endurance aircraft, J. Aircr. 38 (1) (2001) 88–94.
[14] A. Gatto, P. Bourdin, M.I. Friswell, Experimental investigation into articulated winglet effects on flying wing surface pressure aerodynamics, J. Aircr. 47 (5) (2010) 1811–1815.
[15] L. Falcão, A.A. Gomes, A. Suleman, Aero-structural design optimization of a morphing wingtip, J. Intell. Mater. Syst. Struct. 22 (2011) 1113–1124.
[16] E. Daniele, A. Fenza, P.D. Vecchia, Conceptual adaptive wing-tip design for pollution reductions, J. Intell. Mater. Syst. Struct. 23 (2012) 1197–1212.
[17] Jian Sun, Hongliang Gao, Fabrizio Scarpa, Cristian Lira, Yanju Liu, Jinsong Leng, Active inflatable auxetic honeycomb structural concept for morphing wingtips, Smart Mater. Struct. 2014 (23) (2014) 125023.
[18] A. Gatto, F. Mattioni, M.I. Friswell, Experimental investigation of bistable winglets to enhance wing lift takeoff capability, J. Aircr. 46 (2) (2009) 647–655.
[19] F. Mattioni, P.M. Weaver, K.D. Potter, M.I. Friswell, The application of thermally induced multistable composites to morphing aircraft structures, in: Proceeding of SPIE Industrial and Commercial Applications of Smart Structures Technologies 2008, 2008, 693012.
[20] J. Manzo, E. Garcia, Demonstration of an in situ morphing hyperelliptical cambered span wing mechanism, Smart Mater. Struct. 19 (2009) 025012.
[21] K. Saito, F. Agnese, F. Scarpa, A cellular Kirigami morphing wingbox concept, J. Intell. Mater. Syst. Struct. 22 (2011) 935–944.
[22] D. Bornengo, F. Scarpa, C. Remillat, Evaluation of hexagonal chiral structure for morphing airfoil concept, Proc. Inst. Mech. Eng., G J. Aerosp. Eng. 219 (3) (2005) 185–192.
[23] H. Heo, J. Ju, D.M. Kim, Compliant cellular structures: application to a passive morphing airfoil, Compos. Struct. 106 (2013) 560–569.
[24] J. Martin, J.J. Heyder-Bruckner, C. Remillat, F. Scarpa, K. Potter, M. Ruzzene, The hexachiral prismatic wingbox concept, Phys. Status Solidi B 245 (3) (2008) 570–577.
[25] W. Liu, H. Li, Z. Yang, J. Zhang, C. Xiong, Mechanics of a novel cellular structure for morphing applications, Aerosp. Sci. Technol. 95 (2019) 105479.
[26] X. Lachenal, S. Daynes, P.M. Weaver, Review of morphing concepts and materials for wind turbine blade applications, Wind Energy 16 (2013) 283–307.
[27] E.A. Bubert, B.K.S. Woods, K. Lee, C.S. Kothera, N.M. Wereley, Design and fabrication of a passive 1D morphing aircraft skin, J. Intell. Mater. Syst. Struct. 21 (2010) 1699–1717.
[28] R.D. Vocke III, C.S. Kothera, B. Woods, N.M. Wereley, Development and testing of a span-extending morphing wing, J. Intell. Mater. Syst. Struct. 22 (2011) 879–890.
[29] R.D. Vocke III, C.S. Kothera, N.M. Wereley, Development of a span-extending blade tip system for a reconfigurable helicopter rotor, in: 53rd AIAA/ASME/ASCE/AHS/ASC Structures, Structural Dynamics and Materials Conference, 23–26 April 2012, Honolulu, Hawaii, 2012, AIAA 2012-1664.
[30] W.D. Liu, H. Zhu, S.Q. Zhou, Y.L. Bai, Y. Wang, C.S. Zhao, In-plane corrugated cosine honeycomb for 1D morphing skin and its application on variable camber wing, Chin. J. Aeronaut. 26 (4) (2013) 935–942.
[31] S. Barbarino, F. Gandhi, S.D. Webster, Design of extendable chord sections for morphing helicopter rotor blades, J. Intell. Mater. Syst. Struct. 22 (2011) 891–905.
[32] S. Daynes, P.M. Weaver, Design and testing of a deformable wind turbine blade control surface, Smart Mater. Struct. 21 (2012) 105019.
[33] M.R. Hassan, F. Scarpa, M. Ruzzene, N.A. Mohammed, Smart shape memory alloy chiral honeycomb, Materials Science and Engineering: A 481 (2008) 654–657.
[34] Y. Okabe, H. Sugiyama, Shape variable sandwich structure with SMA honeycomb core and CFRP skins, in: Proceeding of SPIE Active and Passive Smart Structures and Integrated Systems 2009, 2009, p. 728817.
[35] D.A. Perkins, J.L. Reed, Havens Jr, Morphing wing structures for loitering air vehicles, in: 45th AIAA/ASME/ASCE/AHS/ASC Structures, Structural Dynamics & Materials Conference, 19-22 April 2004, Palm Springs, California, 2004, AIAA 2004-1888.
[36] A. Spadoni, M. Ruzzene, F. Scarpa, Dynamic response of chiral truss-core assemblies, J. Intell. Mater. Syst. Struct. 17 (11) (2006) 941–952.
[37] H. Abramovitch, M. Burgard, Lucy Edery-Azulay, K.E. Evans, M. Hoffmeister, W. Miller, F. Scarpa, C.W. Smith, Kong-Fah Tee, Smart tetrachiral and hexachiral honeycomb: sensing and impact detection, Compos. Sci. Technol. 70 (7) (2010) 1072–1079.
[38] R. Vos, R. Barrett, Mechanics of pressure-adaptive honeycomb and its application to wing morphing, Smart Mater. Struct. 20 (2011) 094010.
[39] M. Pagitz, E. Lamacchia, J. Hol, Pressure-actuated cellular structures, Bioinspir. Biomim. 7 (2012) 016007.
[40] M. Pagitz, J. Bold, Shape-changing shell-like structures, Bioinspir. Biomim. 8 (2013) 016010.
[41] B. Chang, A. Chew, N. Naghshineh, C. Menon, A spatial bending fluidic actuator: fabrication and quasi-static characteristics, Smart Mater. Struct. 21 (2012) 045008.
[42] S.J. Mazlouman, B. Chang, A. Mahanfar, A. Mahanfar, R.G. Vaughan, C. Menon, Beam-steering antenna using bending fluidic actuators, IEEE Trans. Antennas Propag. 61 (10) (2013) 5287–5290.
[43] J. Berring, K. Kianfar, C. Lira, C. Menon, F. Scarpa, A smart hydraulic joint for future implementation in robotic structures, Robotica 28 (07) (2010) 1045–1056.
[44] C. Menon, C. Lira, Active articulation for future space applications inspired by the hydraulic system of spiders, Bioinspir. Biomim. 1 (2006) 52–61.
[45] S. Schulz, C. Pylatiuk, M. Reischl, J. Martin, R. Mikut, G. Bretthauer, A hydraulically driven multifunctional prosthetic hand, Robotica 23 (2005) 293–299.
[46] C. Thill, J. Etches, I. Bond, K. Potter, P. Weaver, Morphing skins, Aeronaut. J. 3216 (2008) 1–23.
[47] K.R. Olympio, F. Gandhi, L. Asheghian, J. Kudva, Design of a flexible skin for a shear morphing wing, J. Intell. Mater. Syst. Struct. 21 (2010) 1755–1770.
[48] E.A. Bubert, B.K.S. Woods, K. Lee, C.S. Kothera, N.M. Wereley, Design and fabrication of a passive 1D morphing aircraft skin, J. Intell. Mater. Syst. Struct. 21 (2010) 1699–1717.
[49] Y.J. Chen, W.L. Yin, Y.J. Liu, J.S. Leng, Structural design and analysis of morphing skin embedded with pneumatic muscle fibers, Smart Mater. Struct. 20 (2011) 085033.
[50] A. Simpson, J. Jacob, S. Smith, Flight control of a UAV with inflatable wings with wing warping, in: 24th AIAA Applied Aerodynamics Conference, 6 June, 2006, San Francisco, California, 2006, AIAA 2006-2831.
[51] L.W. Kheong, J.D. Jacob, In flight aspect ratio morphing using inflatable wings, in: 46th AIAA Aerospace Sciences Meeting and Exhibit, 7–10 January 2008, Reno, Nevada, 2008, AIAA 2008-425.
[52] J.H. Long Jr., M.E. Hale, M.J. Mchenry, M.W. Westneat, Functions of fish skin flexural stiffness and steady swimming of longnose gar lepisosteus osseus, J. Exp. Biol. 199 (1996) 2139–2151.
[53] S. Barbarino, R. Pecora, L. Lecce, A. Concilio, S. Ameduri, L. De Rosa, Airfoil structural morphing based on SMA actuator series: numerical and experimental studies, J. Intell. Mater. Syst. Struct. 22 (2011) 987–1004.
[54] T. Yokozeki, S. Takeda, T. Ogasawara, T. Ishikawa, Mechanical properties of corrugated composites for candidate materials of flexible wing structures, Composites, Part A 37 (2006) 1578–1586.
[55] C. Thill, J.A. Etches, I.P. Bond, K.D. Potter, P.M. Weaver, Composite corrugated structures for morphing wing skin applications, Smart Mater. Struct. 19 (2010) 124009.
[56] I.K. Kuder, A.F. Arrieta, W.E. Raither, P. Ermanni, Variable stiffness material and structural concepts for morphing applications, Prog. Aerosp. Sci. 63 (2013) 33–55.
[57] J.S. Leng, X. Lan, Y.J. Liu, S.Y. Du, Shape-memory polymers and their composites: stimulus methods and applications, Prog. Mater. Sci. 56 (2011) 1077–1135.
[58] J.L. Reed Jr., C.D. Hemmelgarn, B.M. Pelley, Ernie Havens, Adaptive wing structures, in: Proceedings of SPIE Smart Structures and Materials 2005: Industrial and Commercial Applications of Smart Structures Technologies, 6 March, 2005, San Diego, CA, vol. 5762, 2005, pp. 132–142.
[59] D.R. Bye, P.D. McClure, Design of a morphing vehicle, in: 48th AIAA/ASME/ASCE/AHS/ASC Structures, Structural Dynamics, and Materials Conference, 23 April, 2007, Honolulu, Hawaii, 2007, AIAA 2007-1728.
[60] K. Yu, W.L. Yin, S.H. Sun, Y.J. Liu, J.S. Leng, Design and analysis of morphing wing based on SMP composite, in: Proceeding of SPIE Industrial and Commercial Applications of Smart Structures Technologies 2009, 8 March, 2009, San Diego, California, vol. 7290, 2009, p. 72900S.
[61] W.L. Yin, T. Fu, J.C. Liu, J.S. Leng, Structural shape sensing for variable camber wing using FBG sensors, in: Proceeding of SPIE Sensors and Smart Structures Technologies for Civil, Mechanical, and Aerospace Systems 2009, 8 March, 2009, San Diego, California, vol. 7292, 2009, p. 72921H.
[62] J. Sun, Y.J. Liu, J. Leng, Mechanical properties of shape memory polymer composites enhanced by elastic fibers and their application in variable stiffness morphing skins, J. Intell. Mater. Syst. Struct. (2014), https://doi.org/10.1177/1045389X14546658.
[63] J.N. Grima, K.E. Evans, Auxetic behavior from rotating squares, J. Mater. Sci. Lett. 19 (17) (2000) 1563–1565.
[64] M. Bianchi, F.L. Scarpa, C.W. Smith, Stiffness and energy dissipation in polyurethane auxetic foams, J. Mater. Sci. 43 (17) (2008) 5851–5860.
[65] M. Ruzzene, F. Scarpa, Directional and band-gap behavior of periodic auxetic lattices, Phys. Status Solidi B 242 (3) (2005) 665–680.
[66] R.D. Gregory, F.Y.M. Wan, On plate theories and Saint-Venant's principle, Int. J. Solids Struct. 21 (10) (1985) 1005–1024.
[67] Ning Feng, Liwu Liu, Yangju Liu, Jingsong Leng, A bio-inspired, active morphing skin for camber morphing structures, Smart Mater. Struct. (2015), https://doi.org/10.1088/0964-1726/24/3/035023.
[68] Jian Sun, Fabrizio Scarpa, Yanju Liu, Jinsong Leng, Morphing thickness in airfoils using pneumatic flexible tubes and Kirigami honeycomb, J. Intell. Mater. Syst. Struct. 27 (6) (2016) 755–763.
[69] Y. Chen, W. Yin, Y. Liu, J. Leng, Structural design and analysis of morphing skin embedded with pneumatic muscle fibers, Smart Mater. Struct. 20 (8) (2011).

[70] Ching Ping Chou, Blake Hannaford, Measurement and modeling of McKibben pneumatic artificial muscles, IEEE Int. Conf. Robot. Autom. 12 (1) (1996) 90–102.
[71] E. Jacobs, Airfoil section characteristics as affected by protuberances, NACA Technical Report 446, 1934, pp. 109–124.
[72] R.M. Neville, J. Chen, X. Guo, F. Zhang, W. Wang, Y. Dobah, H. Peng, A Kirigami shape memory polymer honeycomb concept for deployment, Smart Mater. Struct. 26 (5) (2017).